Probing topological signatures in an optically driven α-T_3 lattice

Lakpa Tamang and Tutul Biswas[*]

Department of Physics, University of North Bengal, Raja Rammohunpur-734013, India

The α-T_3 lattice, an interpolation model between the honeycomb lattice of graphene ($\alpha = 0$) and the dice lattice ($\alpha = 1$), undergoes a topological phase transition across $\alpha = 1/\sqrt{2}$ when exposed to a circularly polarized off-resonant light. In this work, several features of the topological transition have been captured via various Berry phase mediated magnetic and thermoelectric effects. For instance, both the Berry curvature and the orbital magnetic moment associated with the flat band change their respective signs across $\alpha = 1/\sqrt{2}$. The orbital magnetization varies linearly with the chemical potential in the forbidden gaps of the quasienergy spectrum. The slope of the orbital magnetization in the gap changes by one unit of e/h as soon as α crosses the value $1/\sqrt{2}$ which is a direct manifestation of the corresponding change in Chern number by one unit. While the anomalous Nernst coefficient vanishes in the gaps, the anomalous Hall conductivity, however, gets quantized in a different manner on either side of $\alpha = 1/\sqrt{2}$. The broken particle-hole symmetry for $0 < \alpha < 1$ offers valley-contrasting features in the thermoelectric coefficients as well as in the orbital magnetization which further open up the possibility to use the underlying driven system in the valley caloritronic applications.

I. INTRODUCTION

Based on the Berry phase effect [1], a new paradigm in condensed matter physics has been developed over last few decades. The Berry phase [2] is a global phase acquired by a Bloch electron while its adiabatic expedition along a closed path in momentum space. It is expressed as a line integral of the Berry connection: $\boldsymbol{A(k)} = i\langle u(\boldsymbol{k})|\nabla_k|u(\boldsymbol{k})\rangle$ over a closed contour in momentum space, where $|u(\boldsymbol{k})\rangle$ is the periodic part of Bloch wave function. The Berry curvature: $\boldsymbol{\Omega(k)} = \nabla_k \times \boldsymbol{A(k)}$ plays an analogous role of magnetic field in momentum space. In the modern theory of condensed matter physics, the Berry phase effect has been regarded as a unifying concept in order to understand a wide variety of intriguing phenomena such as the topological origin of the quantum Hall effect [3], quantized adiabatic pumping [4], the anomalous Hall effect [5–8], electric polarization [9], orbital Magnetization [10–13], spin transport [14,15], the valley Hall effect [16,17], etc. The topological thermoelectric phenomena [18] mediated by the Berry phase has gained considerable interest over the years. Several systems, such as a spin-chiral ferromagnetic Kagome lattice [19], graphene [20], spin-orbit coupled electron/hole doped two-dimensional (2D) semiconductors [21], transition metal dichalcogenides [22,23], topological insulator [24], Weyl semimetals [25–27], etc. exhibit topological signatures in their thermoelectric response, especially in the Nernst coefficients. It is revealed that a gap in the low-energy spectrum despite of its origin is an essential ingredient to observe the topological Nernst effect, especially in the 2D systems. The Nernst effect provides an experimental platform to investigate a wide variety of phenomena such as the detec-tion of vortexlike excitations [28] and charge density waves [29] in cuprate superconductors, anomalous thermoelectric response of graphene [30–32], large Berry curvatures in Dirac semimetals [33], etc. In addition, the Nernst effect has potential technological application in the field of spin caloritronics [34].

The possibility of tuning the low-energy properties of electronic systems dynamically with the help of an external time periodic radiation has opened a new pathway in condensed matter physics nowadays. The notion "Floquet systems" is used synonymously with the periodically driven systems because the nonequilibrium dynamics of the underlying systems are well understood within the framework of the Floquet theory [35]. The radiation-matter interaction in such systems has enormous consequence in the sense that it can induce nontrivial topology in the band structure. The study on light-induced Hall effect in graphene by Oka *et al.* [36] triggered a number of subsequent investigations aiming to probe topological phase transition [37–48], Floquet spin states [49], pseudospin effects [50], dynamical localization [51,52], chiral interfacial modes [53], spin-Hall resonance without a magnetic field [54], etc. in several irradiated systems. More specifically, a circularly polarized light of frequency lying in the off-resonant regime (frequency is high enough compared to any other relevant frequency scale of the system) is able to renormalize the band structure through a second-order virtual photon emission-absorption process. Finally, one gets an effective static Hamiltonian with a gap term whose nature entirely depends on the properties of the external radiation, e.g., intensity, frequency and polarization state. This tunable gap is the central reason behind all photoengineered topological phases as mentioned in the above references. For example, the semimetallic graphene can be transformed into a Chern insulator when illuminated by off-resonant light of

*tbiswas@nbu.ac.in

appropriate frequency [36]. To check how these externally induced topological flavors essentially control the transport properties, a plethora of investigations have been performed on several irradiated systems [40,55–68] in recent years.

In this work, we extract some topological flavors of an irradiated α-T_3 lattice by analyzing the Berry phase mediated magnetic and thermoelectric transport properties. The α-T_3 lattice is identical to a honeycomb lattice or a dice lattice [69–71] when the variable $\alpha \in [0, 1]$ becomes $\alpha = 0$ or $\alpha = 1$, respectively. Several schemes [72–74] have been proposed for a possible experimental realization of the α-T_3 lattice. It is a fast evolving topic of current research as it hosts quasiparticles having pseudospin larger than $S = 1/2$. The Berry phase associated with the adiabatic evolution of the eigenstates depends on α explicitly. This fact is itself manifested in a number of fascinating phenomena including orbital magnetic susceptibility [75], Hall quantization [76,77], Klein tunneling [78,79], Weiss oscillations [80], zitterbewegung [81], plasmons [82–85], peculiar magneto-optical effects [86–89], Ruderman-Kittel-Kasuya-Yosida interaction [90,91], minimal conductivity [92], unconventional topology [93], spin-Hall phase transition [94], etc. When exposed to a time periodic external radiation, the α-T_3 lattice exhibits rich physical phenomena which are reported in a series of recent works [95–99]. In particular, the irradiated system supports a topological phase transition across $\alpha = 1/\sqrt{2}$ [96]. Given this background, it is therefore tempting to investigate the transport properties of an irradiated α-T_3 lattice aiming to extract some topological signatures therein. Very recently, Niu and Wang [100] numerically studied the behavior of the valley polarized current in a circularly polarized light irradiated α-T_3 lattice using the nonequilibrium Green's function formalism. However, the topological aspects of the valley current went largely unaddressed. Here, we study the explicit behaviors of the Berry curvature, the orbital magnetic moment, the orbital magnetization, and anomalous thermoelectric coefficients such as the Nernst coefficient, the anomalous Hall conductivity and the thermal Hall conductivity. It is revealed that all the aforesaid quantities exhibit distinct topological signatures. For example, both the Berry curvature and the orbital magnetic moment associated with the flat band exhibit sign change across $\alpha = 1/\sqrt{2}$. The linear variation of the orbital magnetization and the vanishing anomalous Nernst coefficient when the chemical potential encounters the forbidden gaps are indeed direct topological signatures. The slopes of the linear regions in the orbital magnetization are directly related to the Chern numbers on either side of $\alpha = 1/\sqrt{2}$. Interestingly, we find that the slope of the orbital magnetization for $\alpha > 1/\sqrt{2}$ differs that for $\alpha < 1/\sqrt{2}$ by one unit of e/h, where e is the electronic charge and h is the Planck's constant. This clearly mimics the corresponding change in Chern number by one unit across $\alpha = 1/\sqrt{2}$ to describe the topological transition. The anomalous Hall conductivity also exhibits topological features when the chemical potential is varied in the forbidden gap(s). We also find valley-contrasting features in the observables for $0 < \alpha < 1$ as a direct consequence of the broken particle-hole symmetry. In addition, we obtain some analytical results in the case of an irradiated dice lattice. We find that the undistorted flat band of the driven dice lattice contributes nothing to the Berry curvature. However, the flat band gives
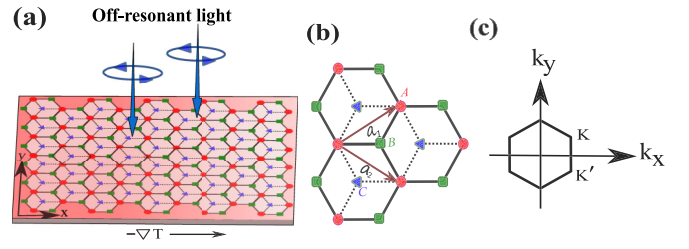

FIG. 1. (a) The bulk portion of the irradiated α-T_3 lattice is schematically shown here. A circularly polarized light is incident on the lattice (located in the x-y plane) normally. The system is subjected to a weak temperature gradient $-\nabla T$ along the x direction. (b) The geometry of the α-T_3 lattice is sketched here. (c) The first Brillouin zone of the α-T_3 lattice. Here, K and K' are the valleys.

rise to a finite orbital magnetic moment which is the sum of the contributions due to the conduction and the valence band. Our results are experimentally detectable and have potential applications in the field of valley caloritronics.

The rest of the paper is organized as follows. In Sec. II, we outline the basic formalism and discuss general features of the quasienergy band structures, the Berry curvature, the orbital magnetic moment, and the orbital magnetization associated with the irradiated α-T_3 lattice. Various aspects of the topological thermoelectric transport are discussed in Sec. III. This paper ends with a summary given in Sec. IV.

II. FORMALISM

We consider the α-T_3 lattice being exposed to a circularly polarized light as shown in Fig. 1(a). We start our discussion by reviewing the essential features [96] of its quasienergy dispersions. We, then, systematically discuss various characteristics of the Berry curvature, the orbital magnetic moment, and the orbital magnetization.

A. Quasienergy

As shown in Fig. 1(b), a unit cell of the α-T_3 lattice includes three inequivalent lattice sites, namely, A, B, and C. The site C, at the center of each hexagon in the honeycomb structure formed by A and B sites, is connected to three A sites only. The lattice translational vectors are given by $\boldsymbol{a}_1 = (3/2, \sqrt{3}/2)a$ and $\boldsymbol{a}_2 = (3/2, -\sqrt{3}/2)a$, where a is the intersite distance. An electron at site B (C) can hop to the site A with an energy cost γ ($\alpha\gamma$), where $\alpha \in [0, 1]$. Therefore $\alpha = 0$ ($\alpha = 1$) corresponds to the case of graphene (dice lattice). Within the nearest-neighbor tight-binding scenario, the static α-T_3 model supports a zero-energy flat band on which the conduction and the valence band touch each other at six Dirac points. Only two of them are independent which represent, furthermore, the valleys K and K' as shown in Fig. 1(c). The low-energy excitations near a Dirac point in a particular valley are governed by the Hamiltonian

$$H_0^\tau(\boldsymbol{k}) = \begin{pmatrix} 0 & f_{\boldsymbol{k}}^\tau \cos\phi & 0 \\ f_{\boldsymbol{k}}^{\tau*} \cos\phi & 0 & f_{\boldsymbol{k}}^\tau \sin\phi \\ 0 & f_{\boldsymbol{k}}^{\tau*} \sin\phi & 0 \end{pmatrix}, \quad (1)$$

where $f_k^\tau = \hbar v_F(\tau k_x - i k_y)$ with $v_F = 3\gamma a/(2\hbar)$ being the Fermi velocity, $\tau = \pm 1$ is the valley index and $\phi = \tan^{-1}(\alpha)$.

We consider a circularly polarized light of frequency ω described by the vector potential $\boldsymbol{A}(t) = A_0(l\cos\omega t, \sin\omega t)$ is incident normally on the α-T_3 lattice. Here, A_0 is the amplitude and l represents the polarization of the light. Now, the minimal coupling between the external radiation and the system modifies the Hamiltonian further as

$$H^\tau(\boldsymbol{k}, t) = \begin{pmatrix} 0 & f_k^\tau(t)\cos\phi & 0 \\ f_k^{\tau*}(t)\cos\phi & 0 & f_k^\tau(t)\sin\phi \\ 0 & f_k^{\tau*}(t)\sin\phi & 0 \end{pmatrix}, \quad (2)$$

where $f_k^\tau(t)$ is obtained from f_k^τ via Pierl's substitution: $\boldsymbol{k} \to \boldsymbol{k} + e\boldsymbol{A}(t)/\hbar$. The modified Hamiltonian $H^\tau(\boldsymbol{k}, t)$ has the same periodicity $T = 2\pi/\omega$ as $\boldsymbol{A}(t)$. The Floquet theory perhaps is the appropriate tool to deal with such time-periodic problem. We consider the so-called off-resonant regime where the frequency of the radiation is much larger than the band width and/or other energy scales of the system under consideration. In this case, one can obtain the following time-independent effective Hamiltonian [101]

$$H_{\text{eff}}^\tau(\boldsymbol{k}) = H_0^\tau(\boldsymbol{k}) + \frac{1}{\hbar\omega}[H_-^\tau(\boldsymbol{k}), H_+^\tau(\boldsymbol{k})] + \mathcal{O}(1/\omega^2), \quad (3)$$

where $H_\pm^\tau(\boldsymbol{k}) = (1/T)\int_0^T e^{\mp i\omega t} H^\tau(\boldsymbol{k}, t)\, dt$. The second term in Eq. (3) is responsible for the virtual photon emission-absorption process which effectively alters the static band structure. Considering terms up to $\mathcal{O}(1/\omega)$, it is straightforward to find the effective Hamiltonian as

$$H_{\text{eff}}^\tau(\boldsymbol{k}) = \begin{pmatrix} \Delta^\tau \cos^2\phi & f_k^\tau\cos\phi & 0 \\ f_k^{\tau*}\cos\phi & -\Delta^\tau\cos 2\phi & f_k^\tau\sin\phi \\ 0 & f_k^{\tau*}\sin\phi & -\Delta^\tau\sin^2\phi \end{pmatrix}, \quad (4)$$

where $\Delta^\tau = \tau l\Delta$ with $\Delta = e^2 A_0^2 v_F^2/\hbar\omega$ is the Haldane-type mass term induced by the off-resonant light. It breaks the time-reversal symmetry and has opposite signs in the two valleys. Diagonalization of $H_{\text{eff}}^\tau(\boldsymbol{k})$ provides the quasienergies as

$$E_\lambda^\tau(\boldsymbol{k}) = 2\sqrt{\frac{-p}{3}}\cos\left[\frac{1}{3}\cos^{-1}\left(\frac{3q}{2p}\sqrt{\frac{-3}{p}}\right) - \frac{2\pi\lambda}{3}\right], \quad (5)$$

where

$$p = -\left[|f_k|^2 + \Delta^2\left(\cos^2 2\phi + \frac{\sin^2 2\phi}{4}\right)\right],$$

$$q = -\tau l\frac{\Delta^3\sin^2 2\phi\cos 2\phi}{4}.$$

Here, $\lambda = 0, 1,$ and 2 are assigned to denote the conduction, the flat, and the valence quasienergy bands, respectively. Equation (5) infers that the application of an off-resonant radiation makes the effective quasienergy dispersion α dependent. The nature of the quasienergy dispersion at the K valley for different values of α are depicted in Fig. 2. We consider the system is being exposed to a right circularly polarized radiation ($l = +1$) and this choice is followed throughout this paper. The effect of the circularly polarized radiation on the band structure of the system is mainly twofold. Firstly, it
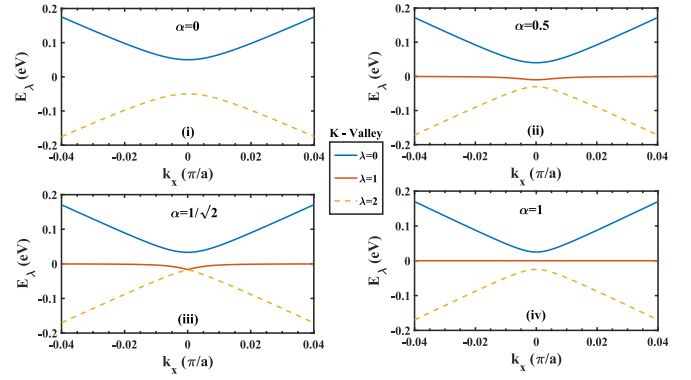

FIG. 2. Quasienergy dispersion at the K valley for different values of α. Here, we consider $\Delta = 50$ meV. It is understood that an external time periodic radiation lifts the degeneracy at $\boldsymbol{k} = 0$ for all values of α except $\alpha = 1/\sqrt{2}$. At this particular value of α, the valence band touches the distorted flat band.

breaks the time-reversal symmetry. Therefore the threefold degeneracy at the Dirac point ($\boldsymbol{k} = 0$) is lifted by opening a gap. However, the scenario corresponding to $\alpha = 1/\sqrt{2}$ is different. Here, the valence band touches the flat band. More specifically, a topological phase transition occurs at $\alpha = 1/\sqrt{2}$ [96]. Secondly, the radiation distorts the flat band in the vicinity of the Dirac point for an intermediate α ($0 < \alpha < 1$). As a result, the particle-hole symmetry is broken. However, the aforesaid symmetry is still preserved for graphene ($\alpha = 0$) as well as for the dice lattice ($\alpha = 1$). For instance, the quasienergy spectrum for an illuminated dice lattice becomes : $E_\pm^{\text{d}}(\boldsymbol{k}) = \pm(\varepsilon_k^2 + \tilde{\Delta}^2)^{1/2}$, $E_0^{\text{d}} = 0$, where $\varepsilon_k = \hbar v_F k$ and $\tilde{\Delta} = \Delta/2$. In other words, the "flatness" of the flat band of a dice lattice is protected against the application of high-frequency radiation. We mention, here, that the particle-hole transformation is associated with the replacement of an electron with wave vector $\boldsymbol{k}$ by a hole with wave vector $\boldsymbol{k}$.

In the quasienergy spectrum corresponding to the K' valley (not shown here), the conduction band touches the distorted flat band at $\alpha = 1/\sqrt{2}$. This feature can also be realized in the K valley by reversing the polarization of radiation ($l = -1$).

B. Berry curvature

The Berry curvature corresponding to a particular Bloch band can be viewed as a kind of "residual" interaction [1] of other nearby bands as the dynamics of the system is locked to a single energy band within the description of the quantum adiabatic theorem. It is well known that the Berry curvature for a two-dimensional system is always directed along the transverse direction. Its gauge-invariant form corresponding to a Bloch band characterized by the indices λ and τ is given by

$$\Omega_\lambda^\tau(\boldsymbol{k}) = -2\hbar^2 \text{Im} \sum_{\lambda' \neq \lambda} \frac{\langle u_\lambda^\tau | v_x | u_{\lambda'}^\tau\rangle\langle u_{\lambda'}^\tau | v_y | u_\lambda^\tau\rangle}{\left[E_\lambda^\tau(\boldsymbol{k}) - E_{\lambda'}^\tau(\boldsymbol{k})\right]^2}, \quad (6)$$

where $u_\lambda^\tau \equiv |u_\lambda^\tau(\boldsymbol{k})\rangle = \sqrt{\mathcal{S}}e^{-i\boldsymbol{k}\cdot\boldsymbol{r}}|\Psi_\lambda^\tau(\boldsymbol{k})\rangle$ is the periodic part of the Bloch state $|\Psi_\lambda^\tau(\boldsymbol{k})\rangle$ with $\mathcal{S}$ as the sample area and $v_i = \hbar^{-1}\nabla_{k_i}H_{\text{eff}}^\tau$ is the effective velocity operator along a particular direction $i = x, y$. It is evident from Eq. (6)
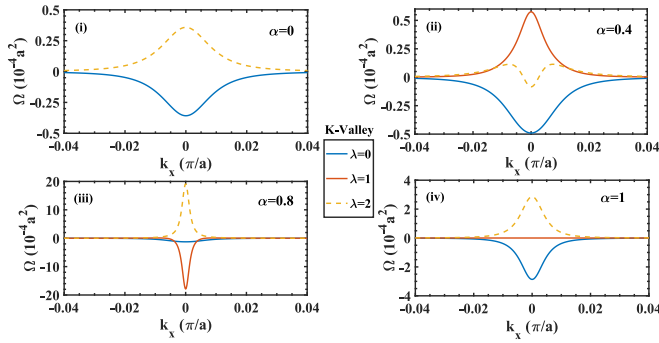
FIG. 3. The distributions of the Berry curvature $\Omega(\mathbf{k})$ near the K valley for different values of α, namely, (i) $\alpha = 0$, (ii) 0.4, (iii) 0.8, and (iv) 1 are shown.

that the Berry curvature becomes singular when there is a degeneracy in the energy spectrum. Under the spatial inversion ($\mathcal{I}$), the particle-hole ($\mathcal{P}$), and the time-reversal ($\mathcal{T}$) operations, the Berry curvature behaves in the following way: $\mathcal{I}^{-1}\Omega_\lambda(\mathbf{k})\mathcal{I} = \Omega_\lambda(-\mathbf{k})$, $\mathcal{P}^{-1}\Omega_{\bar{\lambda}}(\mathbf{k})\mathcal{P} = -\Omega_\lambda(-\mathbf{k})$, and $\mathcal{T}^{-1}\Omega_\lambda(\mathbf{k})\mathcal{T} = -\Omega_\lambda(-\mathbf{k})$, respectively. Here, the index $\bar{\lambda}$ corresponds to the band with quasienergy $-E_\lambda$. A nonvanishing $\Omega(\mathbf{k})$, therefore, demands the breaking of at least one of above mentioned discrete symmetries. For the irradiated α-T_3 lattice, the behavior of the Berry curvature around the K valley is shown in Fig. 3 considering $\Delta = 50$ meV. The Berry curvature for an individual band becomes nonvanishing as a consequence of broken time-reversal symmetry for all values of α. In all cases, $\Omega(\mathbf{k})$ is mostly concentrated near the valley extremum. The Berry curvature for the conduction band is negative for all values of α. It is hard to comment on the topological features from the behavior of $\Omega(\mathbf{k})$ for the conduction band. The Berry curvature for the valence band, however, exhibit nonmonotonic behavior. For $\alpha = 0$, it is positive and peaked at $\mathbf{k} = 0$. A "cusplike" structure with a negative peak value appears when α becomes 0.4. For $\alpha = 0.6$ (not shown here) the Berry curvature becomes negative. The Berry curvature is strongly enhanced and becomes positive when $\alpha = 0.8$. It is still positive if one increases α further to $\alpha = 1$. Here, $\Omega(\mathbf{k})$ changes the sign around $\alpha = 1/\sqrt{2}$ which might be considered as a topological signature. For $0 < \alpha < 1$, the Berry curvature corresponding to the flat band is nonvanishing as a consequence of the particle-hole symmetry breaking. Interestingly, $\Omega(\mathbf{k})$ for the flat band exhibits a sign change across $\alpha = 1/\sqrt{2}$. For the dice lattice ($\alpha = 1$), the contribution of the flat band in $\Omega(\mathbf{k})$ vanishes as the external radiation is unable to break the particle-hole symmetry. It is possible to obtain following analytical expression of $\Omega(\mathbf{k})$ for $\alpha = 1$ as

$$\Omega_\lambda^\tau(\mathbf{k}) = (\lambda - 1)\frac{\hbar^2 v_F^2 \tilde{\Delta}}{\left(\varepsilon_k^2 + \tilde{\Delta}^2\right)^{3/2}}. \tag{7}$$

It is also clear that, at a given $\mathbf{k}$, the total Berry curvature, i.e., the sum of the individual contributions from different bands, vanishes. This is usually known as local conservation of the Berry curvature. In Fig. 4(i) (4(ii)), the peak value of $\Omega(\mathbf{k})$ at $\mathbf{k} = 0$ is depicted over the entire range of α for the $K(K')$ valley. For the K valley, the Berry curvatures corre-
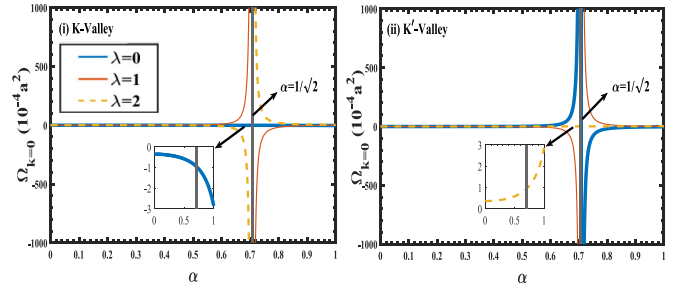

FIG. 4. The peak value of $\Omega(\mathbf{k})$ at $\mathbf{k} = 0$ is plotted as a function of α for the (i) K and (ii) K' valleys. In the K (K') valley, $\Omega(\mathbf{k} = 0)$ for the flat (conduction) band and the valence (flat) band change signs discontinuously across $\alpha = 1/\sqrt{2}$ whereas $\Omega(\mathbf{k} = 0)$ for the conduction (valence) band decreases (increases) monotonically as depicted in the inset. The sign change of the Berry curvature across $\alpha = 1/\sqrt{2}$ might be considered as a topological signature.

sponding to the flat band and the valence band diverge at $\alpha = 1/\sqrt{2}$ while the Berry curvature for the conduction band is finite (as shown in the inset). This divergence is a direct consequence of the fact that the valence band and the flat band touch each other at $\mathbf{k} = 0$ when α becomes $1/\sqrt{2}$ as shown in Fig. 2(iii). As mentioned earlier, $\Omega(\mathbf{k} = 0)$ for the flat (valence) band changes sign from $+ (-)$ to $- (+)$ as α is varied across $\alpha = 1/\sqrt{2}$, thus exhibiting a prominent signature of the topological transition. For the K' valley, $\Omega(\mathbf{k} = 0)$ is finite for the valence band while that corresponding to the conduction band and the flat band encounter divergence at $\alpha = 1/\sqrt{2}$ because the conduction band and the flat band become degenerate at $\mathbf{k} = 0$. The Berry curvatures for the conduction band and the flat band change their respective signs across $\alpha = 1/\sqrt{2}$ as depicted in Fig. 4(ii).

C. Orbital magnetic moment

Another interesting quantity associated with the Bloch band of a given system is the orbital magnetic moment (OMM). The self rotation of an electronic wave packet about the center of mass gives rise to the OMM. The OMM exhibits analogous behavior as the electron spin. In principle, it can be treated as a physical observable because various informations about it can be extracted by studying the magnetic circular dichroism spectrum [102,103]. Generally, it is expressed as

$$\mathbf{m}_\lambda^\tau(\mathbf{k}) = -\frac{ie}{2\hbar}\langle \nabla_k u_\lambda^\tau | \times \left[H_{\text{eff}}^\tau(\mathbf{k}) - E_\lambda^\tau(\mathbf{k}) \right] | \nabla_k u_\lambda^\tau \rangle. \tag{8}$$

The z component of the OMM, however, can be obtained as

$$m_\lambda^\tau(\mathbf{k}) = -\hbar e \, \text{Im} \sum_{\substack{\lambda' \\ (\lambda \neq \lambda')}} \frac{\langle u_\lambda^\tau | v_x | u_{\lambda'}^\tau \rangle \langle u_{\lambda'}^\tau | v_y | u_\lambda^\tau \rangle}{\left[E_\lambda^\tau(\mathbf{k}) - E_{\lambda'}^\tau(\mathbf{k}) \right]}. \tag{9}$$

The symmetry properties of the OMM are as follows: $\mathcal{I}^{-1}m_\lambda(\mathbf{k})\mathcal{I} = m_\lambda(-\mathbf{k})$, $\mathcal{P}^{-1}m_{\bar{\lambda}}(\mathbf{k})\mathcal{P} = m_\lambda(-\mathbf{k})$, and $\mathcal{T}^{-1}m_\lambda(\mathbf{k})\mathcal{T} = -m_\lambda(-\mathbf{k})$. The distribution of the OMM is shown in Fig. 5 for the K valley. The broken time-reversal symmetry gives rise to a nonzero OMM. The OMM is largely concentrated around the valley extremum (i.e., $\mathbf{k} \approx 0$) like the Berry curvature. However, it exhibits some distinct features
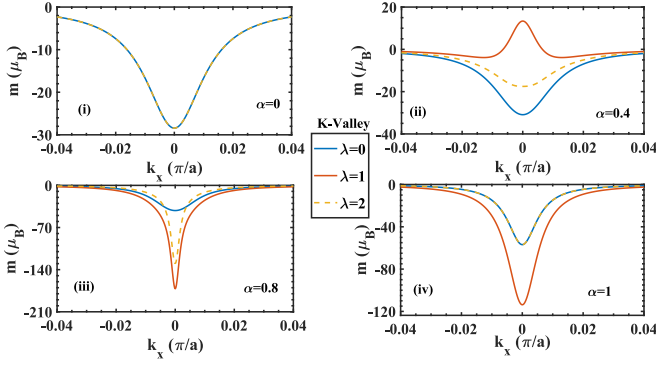
FIG. 5. The distribution of the OMM around the K valley for different values of α considering $\Delta = 50$ meV. For $\alpha = 1$, the flat-band contribution to the OMM does not vanish. Moreover, it is exactly equal to the sum of the individual contributions of the conduction and valence bands.

which are absent in the distribution of the Berry curvature. The OMMs associated with the conduction band and the valence band are negative and they coincide with each other owing to the particle-hole symmetry for both $\alpha = 0$ and $\alpha = 1$. For the dice lattice ($\alpha = 1$), we find that the OMM associated with the flat band is nonvanishing unlike the Berry curvature and it is exactly equal to the sum of the individual contributions from the conduction band and the valence band. This is indeed an interesting result. We find the OMM analytically for $\alpha = 1$ as

$$m_\lambda^\tau(\mathbf{k}) = -\frac{\hbar e v_F^2 \tilde{\Delta}}{2(\varepsilon_k^2 + \tilde{\Delta}^2)}(\delta_{\lambda 0} + 2\delta_{\lambda 1} + \delta_{\lambda 2}). \tag{10}$$

For an intermediate value of α, i.e., $0 < \alpha < 1$, the breaking of the inversion, the particle-hole, and the time-reversal symmetries result in different values of the OMM associated with individual bands. To explore the topological features of the OMM, we show the variation of $m_\lambda^\tau(\mathbf{k} = 0)$ with α for both valleys in Fig. 6. At K valley, the OMMs corresponding to the flat band and the valence band change their respective signs across $\alpha = 1/\sqrt{2}$ while that due to the conduction band decreases monotonically with α. The role of the valence band
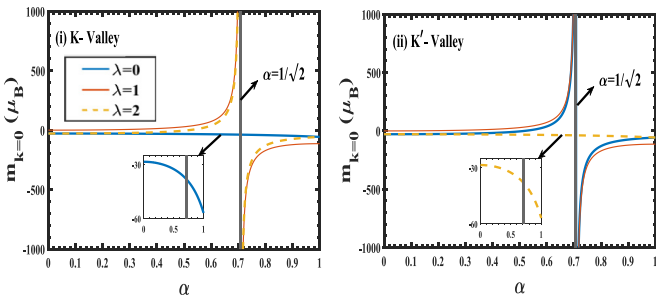

FIG. 6. The peak value of $m(\mathbf{k})$ at $\mathbf{k} = 0$ is plotted as a function of α. (i) In the K valley, the OMMs due to the flat band and the valence band discontinuously change their signs across $\alpha = 1/\sqrt{2}$ whereas that due to the conduction band decreases monotonically with α (as shown in the inset). (ii) The role played by the conduction band in (i) is replaced by the valence band in case of the K' valley.

at K valley is replaced by that of the conduction band at K' valley and vice versa.

D. Orbital magnetization

The orbital magnetization is an interesting bulk property of crystalline materials in which the time-reversal symmetry is broken. In its modern understanding based on either the semiclassical wave packet dynamics of Bloch electrons [10] or the Wannier function approach [11,12] or the perturbation theory [13], it is revealed that the orbital magnetization is comprised of two contributions due to the OMM and the Berry curvature, separately. The free energy of the system in presence of a weak magnetic field $\mathbf{B}$ is given by

$$F^\tau = -\frac{1}{\beta} \sum_{\lambda, \mathbf{k}} \ln[1 + e^{-\beta(\varepsilon_\lambda^\tau(\mathbf{k}) - \mu)}]. \tag{11}$$

Here, $\beta = 1/(k_B T)$, k_B is the Boltzmann constant, T is the temperature, and μ is the chemical potential. Note that the band energy E_λ^τ is modified to $\varepsilon_\lambda^\tau(\mathbf{k}) = E_\lambda^\tau - \mathbf{m}_\lambda^\tau \cdot \mathbf{B}$ as a result of the coupling between the OMM and the magnetic field.

In presence of the Berry curvature, the summation over $\mathbf{k}$ can be converted into an integral as [10]

$$\sum_{\mathbf{k}} \longrightarrow \frac{1}{(2\pi)^2} \int \left(1 + \frac{e\mathbf{B} \cdot \mathbf{\Omega}_\lambda^\tau(\mathbf{k})}{\hbar}\right) d^2k. \tag{12}$$

The Berry curvature essentially modifies the phase-space density of states [the second term in Eq. (12)] as a consequence of the violation of Liouville's theorem in connection with the conservation of the phase-space volume [10].

The orbital magnetization for a particular valley is given by $M_{\text{orb}}^\tau = -(\partial F^\tau/\partial B)_{\mu, T}$ which can be further obtained as $M_{\text{orb}}^\tau = M_{\text{avg}}^\tau + M_{\text{com}}^\tau$, where

$$M_{\text{avg}}^\tau = \frac{1}{(2\pi)^2} \sum_\lambda \int m_\lambda^\tau(\mathbf{k}) f_\lambda^\tau(\mathbf{k}) d^2k, \tag{13}$$

$$M_{\text{com}}^\tau = \frac{e}{2\pi \beta h} \sum_\lambda \int \Omega_\lambda^\tau(\mathbf{k}) \ln[1 + e^{\beta(\mu - E_\lambda^\tau(\mathbf{k}))}] d^2k. \tag{14}$$

Here, $f_\lambda^\tau(\mathbf{k}) = \{1 + \exp[\beta(E_\lambda^\tau(\mathbf{k}) - \mu)]\}^{-1}$ is the Fermi-Dirac distribution function and the integrations in Eqs. (13) and (14) are over the states below the chemical potential μ. Note that M_{avg} is just the thermodynamic average of the OMM and M_{com} is the Berry phase mediated extra term associated with the center of mass motion of the wave packet.

It is possible to find analytical expressions of the orbital magnetization in the case of the irradiated dice lattice ($\alpha = 1$) at very low temperatures. In the limit $T \to 0$, when μ stays in the conduction(+)/valence(−) band, we obtain M_{orb} as

$$M_{\text{orb}}^\pm = \mp \frac{e\mu}{h}\left(1 - \frac{\tilde{\Delta}}{\sqrt{\mu^2 + \tilde{\Delta}^2}}\right) + \frac{e\tilde{\Delta}}{4h} \ln\left|\frac{\mu^2 + \tilde{\Delta}^2}{\tilde{\Delta}^2}\right|. \tag{15}$$

For an intermediate α, i.e., $0 < \alpha < 1$, however, the $\mathbf{k}$ integrations in Eqs. (13) and (14) are evaluated numerically to understand the behavior of M_{orb}. In Fig. 7, the variation of M_{orb} with the chemical potential μ are shown for various values of α, namely, $\alpha = 0$, 0.4, 0.8, and 1 at $T = 100$ K. We consider two values of the light induced energy gap, namely, $\Delta = 50$ meV and $\Delta = 100$ meV. A higher Δ enhances the
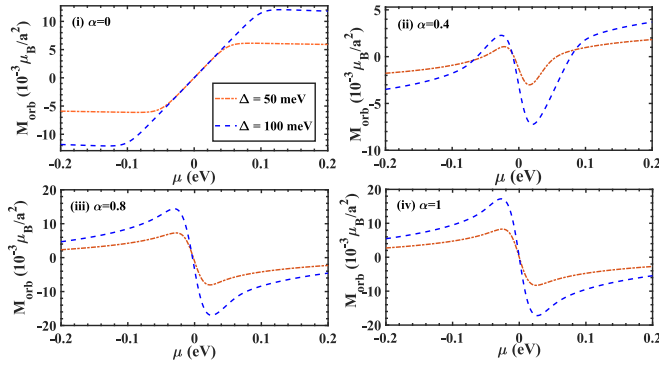
FIG. 7. The orbital magnetization at the K valley as a function of the chemical potential for various values of α considering $T = 100$ K. $M_{\rm orb}$ behaves in antisymmetric manner with μ when $\alpha = 0$ and 1. For $0 < \alpha < 1$, the broken particle-hole symmetry causes a deviation from this behavior.

magnitude of $M_{\rm orb}$ significantly for all values of α. For $\alpha = 0$ [Fig. 7(i)] and $\alpha = 1$ [Fig. 7(iv)], $M_{\rm orb}$ changes antisymmetrically with μ despite of completely different μ dependencies. For example, $M_{\rm orb}$ switches from a negative (positive) value to a positive (negative) value around $\mu = 0$ when $\alpha = 0$ (1). These antisymmetric natures are absent in the cases of $\alpha = 0.4$ [Fig. 7(ii)] and $\alpha = 0.8$ [Fig. 7(iii)] as a consequence of broken particle-hole symmetry.

To extract the topological flavors, we show the μ dependence of the total orbital magnetization which is the sum of contributions from both valleys in the left panel of Fig. 8. We choose lower temperature and higher Δ, namely, $T = 15$ K and $\Delta = 100$ meV in order to visualize the topological signatures in the orbital magnetization. The left panel of Fig. 8 reveals that $M_{\rm orb}^{\rm tot}$ varies linearly with μ in two well separated "windows" Δ_1 and Δ_2 of equal width. Interestingly, Δ_1 is the energy gap between the flat band and the valence band at the K valley, whereas Δ_2 is the band gap between the conduction band and the flat band at the K' valley as depicted in the right panel of Fig. 8. Note that the widths of the "windows" strongly depend on α. We find $\Delta_1 = 58.62$ meV when $\alpha = 0.4$ and $\Delta_1 = 34.25$ meV for $\alpha = 0.9$. The linear portions of $M_{\rm orb}^{\rm tot}$ are determined by the Berry phase mediated term $M_{\rm com}^{\rm tot}$. We
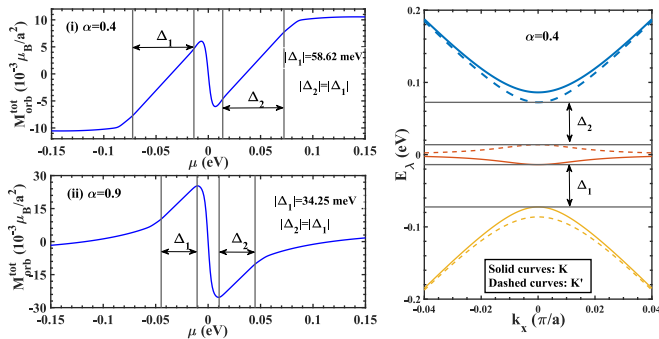

FIG. 8. (Left) The μ-dependence of the total orbital magnetization, i.e., sum of the contributions from both valleys for (i) $\alpha = 0.4$ and (ii) $\alpha = 0.9$. (Right) Quasienergy dispersion for both valleys when $\alpha = 0.4$. Here, we consider $T = 15$ K and $\Delta = 100$ meV.
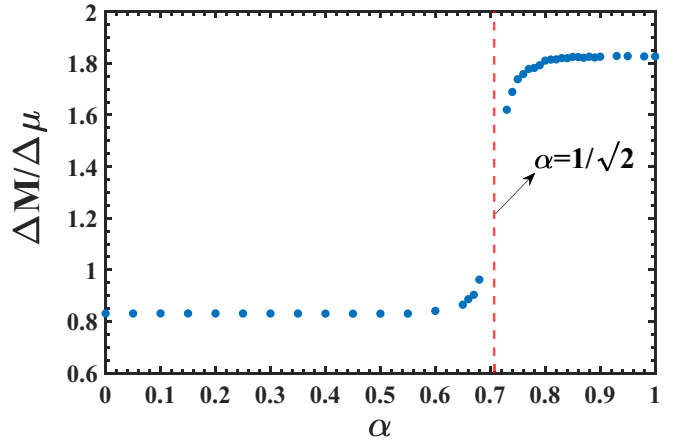

FIG. 9. Slope of the orbital magnetization (in units of e/h) in the band gap for the entire range of α. The values of the parameters are chosen same as in Fig. 8. It is clear that the slope changes by one unit of e/h across $\alpha = 1/\sqrt{2}$.

have checked that (not shown here) $M_{\rm avg}^{\rm tot}$ exhibits plateaus of different heights when μ encounters the band gaps. The linear variation of $M_{\rm orb}^{\rm tot}$ with μ in the forbidden gap(s) is indeed a topological signature which can be understood from the following relation [12]:

$$\frac{dM_{\rm orb}^{\rm tot}}{d\mu} = \frac{e}{h} \sum_{\lambda}^{\rm occ} C_\lambda, \tag{16}$$

where the summation is over the occupied bands and C_λ is the Chern number corresponding to the quasienergy band index λ. As mentioned earlier, an irradiated α-T_3 lattice undergoes a topological phase transition across $\alpha = 1/\sqrt{2}$ [96], which is characterized by a change in the Chern number by one unit from $(C_0, C_1, C_2) = (-1, 0, 1)$ to $(C_0, C_1, C_2) = (-2, 0, 2)$. This fact is reflected in the corresponding change in the slope of the orbital magnetization in the band gaps. As estimated from Fig. 8, the slope of $M_{\rm orb}^{\rm tot}$ for $\alpha = 0.9$ differs from that for $\alpha = 0.4$ by one unit of e/h. It is noteworthy that the slopes of the linear regions in Δ_1 and Δ_2 are same for both values of α. This can be explained as follows. For instance, for $\alpha = 0.4$, when μ is varied in Δ_1, only the valence band is occupied for which the Chern number is 1. Then, Eq. (16) confirms the linear variation of $M_{\rm orb}^{\rm tot}$ with μ in the energy gap Δ_1. On the other hand, when μ is tuned in the gap Δ_2, both the flat and the valence bands are occupied. As the Chern number corresponding to the flat band is 0, it is easy to conclude that $M_{\rm orb}^{\rm tot}$ should vary linearly with μ with the same slope as that in Δ_1. Similar argument will also hold in the case of $\alpha = 0.9$. The peculiar behavior of $M_{\rm orb}^{\rm tot}$ when μ is tuned in the region between the "windows" Δ_1 and Δ_2 is entirely attributed to the distorted flat band. In addition, we extract the slope of the orbital magnetization in the band gap over a full range of α as shown in Fig. 9. The change in slope by one unit of e/h across $\alpha = 1/\sqrt{2}$ is a clear indication of the topological transition. In Fig. 10, we show the dependence of $M_{\rm orb}$ on μ for both valleys. For $\alpha = 0$ and 1, we find that $M_{\rm orb}$ at the K valley coincides with that at the K' valley as a result of the particle-hole symmetry. However, for $0 < \alpha < 1$, the
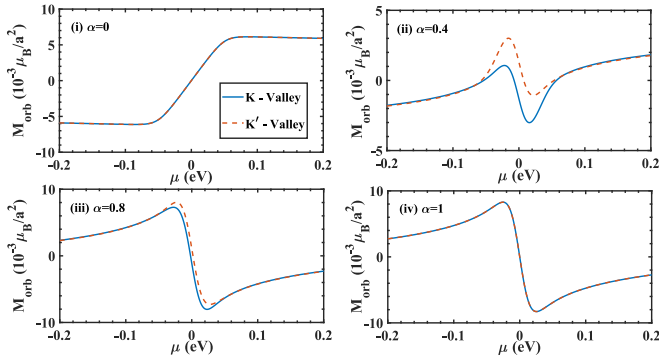
FIG. 10. Orbital magnetization as function of μ for both valleys considering $\Delta = 50$ meV and $T = 100$ K. The valleys contribute identically to M_{orb} for both $\alpha = 0$ and $\alpha = 1$ owing to the particle-hole symmetry. However, breaking of that symmetry introduces the valley-contrasting features in M_{orb} when $0 < \alpha < 1$.

breaking of both particle-hole and time-reversal symmetries lead to a valley-contrasting M_{orb} as shown in Figs. 10(ii) and 10(iii).

III. ANOMALOUS THERMOELECTRIC COEFFICIENTS

In this Sec., we intend to study the Berry phase mediated Nernst-Ettingshausen and Righi-Leduc effects in an irradiated $\alpha\text{-}T_3$ lattice. We focus on the behavior of relevant thermoelectric coefficients, mainly the Nernst and the thermal conductivity tensors $\overleftrightarrow{\alpha}$ and $\overleftrightarrow{\kappa}$, respectively. The conventional Nernst effect is associated with the generation of a transverse voltage in the presence of a temperature gradient and an external magnetic field. However, it is possible to detect the Nernst signal in the absence of a magnetic field. This is usually known as the anomalous Nernst effect (ANE). Here, a nontrivial Berry curvature plays a role of an effective magnetic field in the reciprocal space so that the charge carrier gets a transverse anomalous velocity. One can manipulate the finite spread of a wave packet representing a charge carrier to develop a semiclassical theory of anomalous thermoelectric transport phenomena. It is demonstrated that a Berry-phase correction term in the orbital magnetization plays an important role in the ANE [18]. For a particular valley, the expressions for the anomalous Nernst coefficient (ANC), and the thermal Hall conductivity (THC), are, respectively, given by [18,104]

$$\alpha_{xy}^{\tau} = -\frac{k_B e}{h} \sum_{\lambda} \int \frac{d^2k}{(2\pi)^2} \, \Omega_{\lambda}^{\tau}(\boldsymbol{k}) \big\{ \beta \big(E_{\lambda}^{\tau} - \mu\big) f_{\lambda}^{\tau}(\boldsymbol{k})$$
$$+ \ln\big[1 - f_{\lambda}^{\tau}(\boldsymbol{k})\big]\big\} \tag{17}$$

and

$$\kappa_{xy}^{\tau} = \frac{k_B^2 T}{h} \sum_{\lambda} \int \frac{d^2k}{(2\pi)^2} \, \Omega_{\lambda}^{\tau}(\boldsymbol{k}) \bigg\{ \frac{\pi^2}{3} + \beta^2 \big(E_{\lambda}^{\tau} - \mu\big)^2 f_{\lambda}^{\tau}(\boldsymbol{k})$$
$$- 2\mathrm{Li}_2\big[1 - f_{\lambda}^{\tau}(\boldsymbol{k})\big] - \big[\ln\big(1 + e^{-\beta(E_{\lambda}^{\tau} - \mu)}\big)\big]^2 \bigg\}. \tag{18}$$

Here, $\mathrm{Li}_2(z)$ is the polylogarithmic function. The quantity within the curly bracket in Eq. (17) can be identified as the entropy density $S_{\lambda}^{\tau}(\boldsymbol{k}) = -f_{\lambda}^{\tau}(\boldsymbol{k}) \ln[f_{\lambda}^{\tau}(\boldsymbol{k})] - [1 - f_{\lambda}^{\tau}(\boldsymbol{k})]$
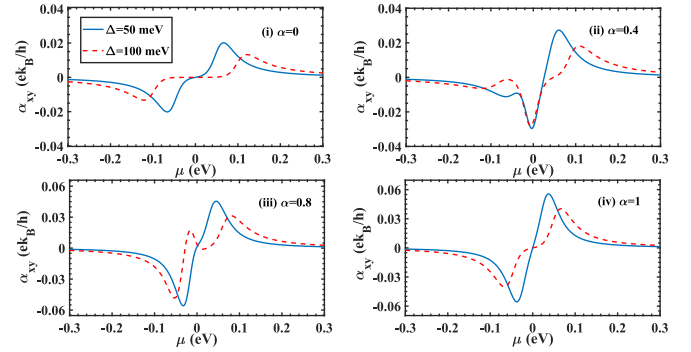
FIG. 11. The variation of α_{xy} as a function of μ for various values of α at the K valley considering $T = 100$ K. α_{xy} exhibits antisymmetric variation with μ for $\alpha = 0, 1$. However, there is a significant deviation from this behavior when $0 < \alpha < 1$ as a result of the broken particle-hole symmetry.

$\ln[1 - f_{\lambda}^{\tau}(\boldsymbol{k})]$. An entropy generation around the Fermi surface and the Berry curvature both can control the behavior of α_{xy}. Therefore α_{xy} becomes very much sensitive to any changes in the Fermi surface properties such as the Fermi energy, temperature, etc. However, the Berry curvature alone determines the anomalous Hall conductivity(AHC) as given by [5,105]

$$\sigma_{xy}^{\tau} = \frac{e^2}{\hbar} \sum_{\lambda} \int \frac{d^2k}{(2\pi)^2} \, \Omega_{\lambda}^{\tau}(\boldsymbol{k}) f_{\lambda}^{\tau}(\boldsymbol{k}). \tag{19}$$

In the $T \to 0$ limit, Eqs. (17) and (18) reduce to the following Mott relation and Widemann-Franz law, respectively:

$$\alpha_{xy}^{\tau} = -\frac{\pi^2 k_B^2 T}{3e} \frac{d\sigma_{xy}^{\tau}}{d\mu} \tag{20}$$

and

$$\kappa_{xy}^{\tau} = \frac{\pi^2 k_B^2 T}{3e^2} \sigma_{xy}^{\tau}. \tag{21}$$

Before discussing the numerical results, we now focus on some analytical results for the irradiated dice lattice ($\alpha = 1$) obtained at very low temperature. When the chemical potential lies in the conduction band $(+)$/valence band $(-)$, we find

$$\sigma_{xy}^{\pm} = \mp \frac{e^2}{h} \left(1 - \frac{\tilde{\Delta}}{\sqrt{\mu^2 + \tilde{\Delta}^2}} \right). \tag{22}$$

When μ falls in the band gap, the AHC becomes $\sigma_{xy}^0 = \frac{e^2}{h}$. When μ lies within either conduction band or valence band, we find $\alpha_{xy}^{\pm} = \pm\frac{\pi k_B e T \tilde{\Delta}}{6h\mu^2}$, and $\alpha_{xy} = 0$ otherwise.

The ANC α_{xy} is evaluated numerically from Eq. (17) and its dependence on the chemical potential μ at $T = 100$ K is depicted in Fig. 11 for the K valley. A higher Δ reduces the magnitude of α_{xy} for all values of α. It also causes a shift in the position of the peak towards higher values of μ. It is evident from Figs. 11(i) and 11(iv), as μ is varied from the valence band to the conduction band, α_{xy} shows the antisymmetric behavior with a zero value plateau in the band gap for $\alpha = 0$ and $\alpha = 1$, respectively. However, the plateau corresponding to $\Delta = 50$ meV and $\alpha = 1$ is not visible [Fig. 11(iv)] because
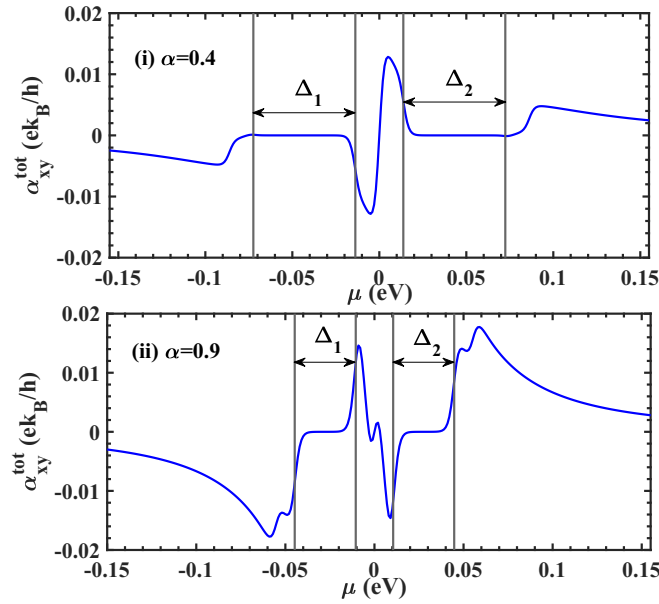
FIG. 12. Plot of $\alpha_{xy}^{\mathrm{tot}}$ vs μ at $T = 20$ K for the K valley considering $\Delta = 100$ meV. $\alpha_{xy}^{\mathrm{tot}}$ vanishes in the forbidden gaps Δ_1 and Δ_2. For $\alpha = 0.4$, $\alpha_{xy}^{\mathrm{tot}}$ changes sign once from negative to positive when μ is varied in the region between Δ_1 and Δ_2. However, $\alpha_{xy}^{\mathrm{tot}}$ changes its sign several times when $\alpha = 0.9$.

the higher thermal energy washes away it in this particular case. These plateaus would be more noticeable at lower temperatures. The width of the plateau is proportional to the photoinduced band gap. The width of the plateau for $\alpha = 1$ becomes half of that for $\alpha = 0$. This is due to the fact that the photoinduced band gap for the dice lattice is exactly half of that for an irradiated graphene. The vanishing of α_{xy} in the forbidden gap is connected with both the entropy density $S(\boldsymbol{k})$ and the Berry curvature $\Omega(\boldsymbol{k})$. As depicted in Fig. 3, $\Omega(\boldsymbol{k})$ is mostly concentrated in the band gap at $\boldsymbol{k} = 0$ and dying out on either side. On the other hand, at very low temperature, $S(\boldsymbol{k})$ is sharply peaked at the Fermi surface and vanishes for completely filled and completely empty bands. For μ slightly above and below, the band gap, the intersection of the Fermi surface and the states with nonzero Berry curvature yield a finite contribution to α_{xy} which differs in a sign for μ below and above the band gap due to the sign change of the Berry curvature. As one approaches the band gap from either side, the Berry curvature starts growing and attains a sharp peak in the band gap near $\boldsymbol{k} = 0$, however, the entropy density carries no weight resulting in a vanishing α_{xy} in the band gap.

The broken particle-hole symmetry corresponding to an intermediate $\alpha(\neq 0, 1)$ makes the scenario more interesting. In this case, additional peaks/dips appear in α_{xy} as μ scans the energy bands [see Figs. 11(ii) and 11(iii)]. The plateau(s) in the band gap(s) will be prominent at higher Δ and lower temperature. In Fig. 12, we show the μ dependence of total ANC $\alpha_{xy}^{\mathrm{tot}}$ i.e., sum of individual contributions from both valleys for (i) $\alpha = 0.4$ and (ii) 0.9 considering $T = 20$ K and $\Delta = 100$ meV. In Fig. 12(i), we notice that $\alpha_{xy}^{\mathrm{tot}}$ remains at zero in two distinct "windows" of μ. As mentioned in the discussion of the orbital magnetization, these windows are basically Δ_1 and Δ_2. Near the edges of each window, the plateaus in $\alpha_{xy}^{\mathrm{tot}}$ are smeared out due to finite temperature.
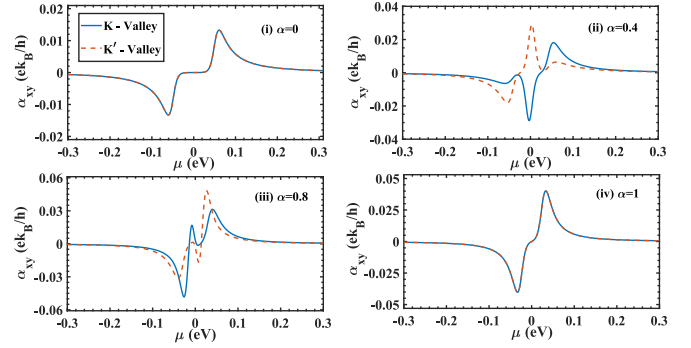

FIG. 13. Plot of α_{xy} vs μ at $T = 50$ K for both valleys considering $\Delta = 50$ meV. α_{xy} exhibits valley-contrasting physics at an intermediate α, i.e., $0 < \alpha < 1$ due to broken particle-hole symmetry.

The behavior of $\alpha_{xy}^{\mathrm{tot}}$ in the region between the windows for $\alpha = 0.4$ and 0.9 are completely different. For $\alpha = 0.4$, $\alpha_{xy}^{\mathrm{tot}}$ changes its sign once from negative to positive. On the other hand, it changes several times when $\alpha = 0.9$.

The μ dependence of α_{xy} is shown for both valleys in Fig. 13 considering $\Delta = 50$ meV and $T = 50$ K. As depicted in Figs. 13(i) and 13(iv), the Nernst coefficient is independent of the valley index τ for $\alpha = 0$ and 1. This can be readily understood from Eq. (17) with the aid of Eq. (7) for $\alpha = 1$. This is a direct consequence of the particle-hole symmetry and valley degeneracy. However, the valley-contrasting behavior of α_{xy} is revealed for $0 < \alpha < 1$ [Figs. 13(ii) and 13(iii)] as a result of broken particle-hole and valley symmetry.

The AHC σ_{xy} is calculated numerically from Eq. (19) and its variation with the chemical potential at $T = 50$ K is shown in Fig. 14. Since the inversion as well as the particle-hole symmetry is preserved for both graphene and the dice lattice, we find that the Hall conductivities for both the valleys coincide when $\alpha = 0$ and $\alpha = 1$. As μ is varied in the band gap, in both cases, all the occupied states in the valence band contribute to σ_{xy} which results in a plateau of width proportional to the gap. Note that the flat band contributes nothing to σ_{xy} because the corresponding Berry curvature vanishes. The height of the plateau for $\alpha = 1$ is twice of that corresponding to $\alpha = 0$. For $\alpha \neq 0, 1$, the system does not possess the inversion and the particle-hole symmetry, resulting in valley-contrasting features in the behavior of σ_{xy}. In this case, the "two-plateau"
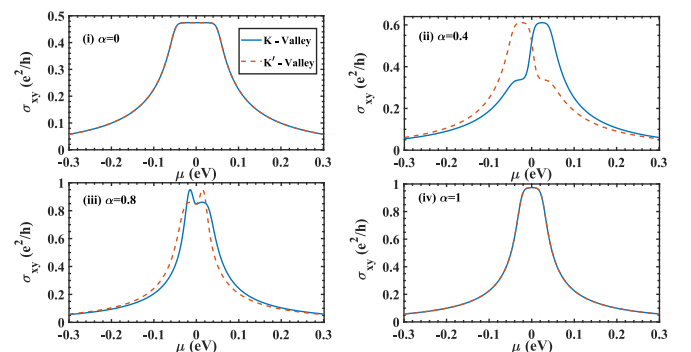

FIG. 14. Plot of σ_{xy} vs μ at $T = 50$ K for both valleys considering $\Delta = 50$ meV. Valley-contrasting features in σ_{xy} are realized for $0 < \alpha < 1$.
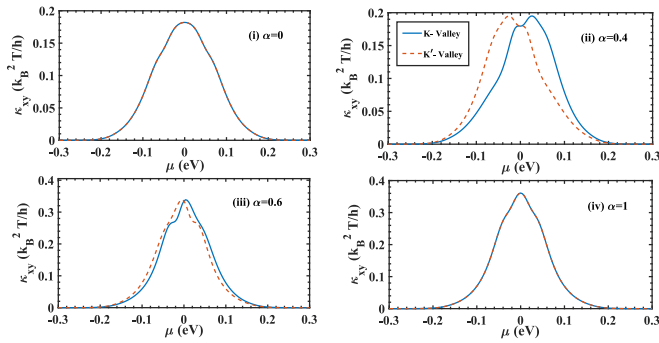
FIG. 15. Plot of κ_{xy} vs μ at $T = 100$ K for both valleys considering $\Delta = 50$ meV. The valley-contrasting features appear in κ_{xy} only when $0 < \alpha < 1$ as a consequence of the broken particle-hole symmetry.

structure is observed as a result of the existence of two band gaps of unequal size in the quasienergy spectrum at each valley. These features will be more noticeable at lower temperature and higher Δ. The total AHC, i.e., sum of the individual contributions from each valley, however, would display interesting features (not shown here explicitly). As evident from Fig. 14, the total AHC would approach the quantized value e^2/h ($2e^2/h$) approximately in the band gaps Δ_1 and Δ_2 when $\alpha < 1/\sqrt{2}$ ($\alpha > 1/\sqrt{2}$), thus validating a topological phase transition across $\alpha = 1/\sqrt{2}$. This quantized nature of σ_{xy} leads to a vanishing α_{xy} in the band gap as evident using Eq. (20).

Using Eq. (18), we calculate the THC κ_{xy} numerically. Its variation with μ at both valleys are shown in Fig. 15 considering $T = 100$ K and $\Delta = 50$ meV. For $\alpha = 0, 1$, κ_{xy} behaves as an even function of μ unlike α_{xy}, owing to the particle-hole symmetry. The THC exhibits similar features as σ_{xy} and this similarity would be more prominent at lower temperatures as a validation of the Mott relation. However, κ_{xy} vanishes away from the band gap regions, i.e., deep in the valence band or the conduction band. For $0 < \alpha < 1$, the valley-contrasting features are also available in κ_{xy}.

IV. SUMMARY

In summary, we have explored the topological signatures of the irradiated α-T_3 lattice via various Berry phase effects. Ex-

plicitly, we calculate the Berry curvature, the orbital magnetic moment, the orbital magnetization and the anomalous thermoelectric coefficients. All these quantities display distinct topological characteristics which can be captured experimentally. The Berry curvature as well as the orbital magnetic moment associated with the flat band display a sign-change across $\alpha = 1/\sqrt{2}$. The light induced distortion of the flat band near the Dirac points essentially introduces two well separated α-dependent forbidden gaps of equal width. The orbital magnetization exhibits linear dependence on the chemical potential in the forbidden gaps. The slope of the orbital magnetization in the band gap changes by one unit of e/h across $\alpha = 1/\sqrt{2}$ which can be considered as a direct manifestation of the change in the Chern number by one unit. The anomalous Nernst coefficient, however, vanishes when the chemical potential is varied in the band gaps. The anomalous Hall conductivity attains a plateau whenever the chemical potential falls in the band gap. For $0 < \alpha < 1$, a "two-plateau" structure in the Hall conductivity is observed at individual valleys. However, the total anomalous Hall conductivity in the band gaps approaches e^2/h and $2e^2/h$, approximately when $\alpha < 1/\sqrt{2}$ and $\alpha > 1/\sqrt{2}$, respectively. The thermal Hall conductivity follows the anomalous Hall conductivity in a similar way. For $0 < \alpha < 1$, the broken particle-hole symmetry introduces the valley-contrasting features in the orbital magnetization and the thermoelectric coefficients. These features essentially suggest that the driven α-T_3 lattice could be used as a potential ingredient in valley caloritronic devices. We obtain closed analytical expressions of the above mentioned quantities in the case of the irradiated dice lattice ($\alpha = 1$). The analytical results are valley independent owing to the particle-hole as well as the inversion symmetry. The Berry curvature associated with the flat band vanishes whereas the flat band contributes a significant amount to the orbital magnetic moment. Moreover, the contribution of the flat band in the orbital magnetic moment is the sum of individual contributions coming from the conduction and the valence bands.

[1] D. Xiao, M. C. Chang, and Q. Niu, Berry phase effects on electronic properties, Rev. Mod. Phys. **82**, 1959 (2010).

[2] M. V. Berry, Quantal phase factors accompanying adiabatic changes, Proc. R. Soc. Lond. A **392**, 45 (1984).

[3] D. J. Thouless, M. Kohmoto, M. P. Nightingale, and M. den Nijs, Quantized Hall Conductance in a Two-Dimensional Periodic Potential, Phys. Rev. Lett. **49**, 405 (1982).

[4] D. J. Thouless, Quantization of particle transport, Phys. Rev. B **27**, 6083 (1983).

[5] T. Jungwirth, Q. Niu, and A. H. MacDonald, Anomalous Hall Effect in Ferromagnetic Semiconductors, Phys. Rev. Lett. **88**, 207208 (2002).

[6] Z. Fang, N. Nagaosa, K. S. Takahashi, A. Asamitsu, R. Mathieu, T. Ogasawara, H. Yamada, M. Kawasaki, Y. Tokura, and K. Terakura, The anomalous hall effect and magnetic monopoles in momentum space, Science **302**, 92 (2003).

[7] Y. Yao, L. Kleinman, A. H. MacDonald, J. Sinova, T. Jungwirth, D.-S. Wang, E. Wang, and Q. Niu, First Principles Calculation of Anomalous Hall Conductivity in Ferromagnetic bcc Fe, Phys. Rev. Lett. **92**, 037204 (2004).

[8] F. D. M. Haldane, Berry Curvature on the Fermi Surface: Anomalous Hall Effect as a Topological Fermi-Liquid Property, Phys. Rev. Lett. **93**, 206602 (2004).

[9] R. D. King-Smith and D. Vanderbilt, Theory of polarization of crystalline solids, Phys. Rev. B **47**, 1651(R) (1993).

[10] D. Xiao, J. Shi, and Q. Niu, Berry Phase Correction to Electron Density of States in Solids, Phys. Rev. Lett. **95**, 137204 (2005).

[11] T. Thonhauser, D. Ceresoli, D. Vanderbilt, and R. Resta, Orbital Magnetization in Periodic Insulators, Phys. Rev. Lett. **95**, 137205 (2005).

[12] D. Ceresoli, T. Thonhauser, D. Vanderbilt, and R. Resta, Orbital magnetization in crystalline solids: Multi-band insulators, Chern insulators, and metals, Phys. Rev. B **74**, 024408 (2006).

[13] J. Shi, G. Vignale, D. Xiao, and Q. Niu, Quantum Theory of Orbital Magnetization and Its Generalization to Interacting Systems, Phys. Rev. Lett. **99**, 197202 (2007).

[14] S. Murakami, N. Nagaosa, and S.-C. Zhang, Dissipationless quantum spin current at room temperature, Science **301**, 1348 (2003).

[15] J. Sinova, D. Culcer, Q. Niu, N. A. Sinitsyn, T. Jung-wirth, and A. H. MacDonald, Universal Intrinsic Spin Hall Effect, Phys. Rev. Lett. **92**, 126603 (2004).

[16] D. Xiao, W. Yao, and Q. Niu, Valley-Contrasting Physics in Graphene: Magnetic Moment and Topological Transport, Phys. Rev. Lett. **99**, 236809 (2007).

[17] D. Xiao, G.-B. Liu, W. Feng, X. Xu, and W. Yao, Coupled Spin and Valley Physics in Monolayers of MoS_2 and Other Group-VI Dichalcogenides, Phys. Rev. Lett. **108**, 196802 (2012).

[18] D. Xiao, Y. Yao, Z. Fang, and Q. Niu, Berry-Phase Effect in Anomalous Thermoelectric Transport, Phys. Rev. Lett. **97**, 026603 (2006).

[19] Z. Wang and P. Zhang, Orbital magnetization and its effects in spin-chiral ferromagnetic kagome lattice, Phys. Rev. B **76**, 064406 (2007).

[20] C. Zhang, S. Tewari, and S. Das Sarma, Berry-phase-mediated topological thermoelectric transport in gapped single and bilayer graphene, Phys. Rev. B **79**, 245424 (2009).

[21] E. Dumitrescu, C. Zhang, D. C. Marinescu, and S. Tewari, Topological thermoelectric effects in spin-orbit coupled electron- and hole-doped semiconductors, Phys. Rev. B **85**, 245301 (2012).

[22] G. Sharma, Tunable topological Nernst effect in two-dimensional transition-metal dichalcogenides, Phys. Rev. B **98**, 075416 (2018).

[23] V. Vargiamidis, P. Vasilopoulos, M. Tahir, and N. Neophytou, Berry curvature, orbital magnetization, and Nernst effect in biased bilayer WSe_2, Phys. Rev. B **102**, 235426 (2020).

[24] T. Yokoyama and S. Murakami, Transverse magnetic heat transport on the surface of a topological insulator, Phys. Rev. B **83**, 161407(R) (2011).

[25] R. Lundgren, P. Laurell, and G. A. Fiete, Thermoelectric properties of Weyl and Dirac semimetals, Phys. Rev. B **90**, 165115 (2014).

[26] G. Sharma, P. Goswami, and S. Tewari, Nernst and magnetothermal conductivity in a lattice model of Weyl fermions, Phys. Rev. B **93**, 035116 (2016).

[27] G. Sharma, C. Moore, S. Saha, and S. Tewari, Nernst effect in dirac and inversion-asymmetric weyl semimetals, Phys. Rev. B **96**, 195119 (2017).

[28] Z. A. Xu, N. P. Ong, Y. Wang, T. Kakeshita, and S. Uchida, Vortex-like excitations and the onset of superconducting phase fluctuation in underdoped $La_{2-x}Sr_xCuO_4$, Nature (London) **406**, 486 (2000).

[29] R. Bel and K. Behnia, Ambipolar Nernst Effect in $NbSe_2$, Phys. Rev. Lett. **91**, 066602 (2003).

[30] P. Wei, W. Bao, Y. Pu, C. N. Lau, and J. Shi, Anomalous Thermoelectric Transport of Dirac Particles in Graphene, Phys. Rev. Lett. **102**, 166808 (2009).

[31] Y. M. Zuev, W. Chang, and P. Kim, Thermoelectric and Magnetothermoelectric Transport Measurements of Graphene, Phys. Rev. Lett. **102**, 096807 (2009).

[32] J. G. Checkelsky and N. P. Ong, Thermopower and nernst effect in graphene in a magnetic field, Phys. Rev. B **80**, 081413(R) (2009).

[33] T. Liang, J. Lin, Q. Gibson, T. Gao, M. Hirschberger, M. Liu, R. J. Cava, and N. P. Ong, Anomalous Nernst Effect in the Dirac Semimetal Cd_3As_2, Phys. Rev. Lett. **118**, 136601 (2017).

[34] X. Q. Yu, Z. G. Zhu, G. Su, and A. P. Jauho, Thermally Driven Pure Spin and Valley Currents via the Anomalous Nernst Effect in Monolayer Group-VI Dichalcogenides, Phys. Rev. Lett. **115**, 246601 (2015).

[35] G. Floquet, Sur les equations differentielles lineaires a co-efficients periodiques, Ann. Sci. Ec. Norm. Super. **12**, 47 (1883).

[36] T. Oka and H. Aoki, Photovoltaic hall effect in graphene, Phys. Rev. B **79**, 081406(R) (2009).

[37] J. I. Inoue and A. Tanaka, Photoinduced Transition between Conventional and Topological Insulators in Two-Dimensional Electronic Systems, Phys. Rev. Lett. **105**, 017401 (2010).

[38] T. Kitagawa, E. Berg, M. Rudner, and E. Demler, Topological characterization of periodically driven quantum systems, Phys. Rev. B **82**, 235114 (2010).

[39] N. H. Lindner, G. Refael, and V. Galitski, Floquet topological insulator in semiconductor quantum wells, Nat. Phys. **7**, 490 (2011).

[40] T. Kitagawa, T. Oka, A. Brataas, L. Fu, and E. Delmer, Transport properties of nonequilibrium systems under the application of light: Photoinduced quantum Hall insulators without Landau levels, Phys. Rev. B **84**, 235108 (2011).

[41] J. I. Inoue and A. Tanaka, Photoinduced spin chern number change in a two-dimensional quantum spin Hall insulator with broken spin rotational symmetry, Phys. Rev. B **85**, 125425 (2012).

[42] M. Ezawa, Photoinduced Topological Phase Transition and a Single Dirac-Cone State in Silicene, Phys. Rev. Lett. **110**, 026603 (2013).

[43] J. Cayssol, B. Dora, F. Simon, and R. Moessner, Floquet topological insulators, Phys. Stat. Sol. RRL **7**, 101 (2013).

[44] P. Delplace, A. G. Leon, and G. Platero, Merging of dirac points and floquet topological transitions in ac-driven graphene, Phys. Rev. B **88**, 245422 (2013).

[45] P. M. Perez-Piskunow, G. Usaj, C. A. Balseiro, and L. E. F. F. Torres, Floquet chiral edge states in graphene, Phys. Rev. B **89**, 121401(R) (2014).

[46] X. Zhai and G. Jin, Photoinduced topological phase transition in epitaxial graphene, Phys. Rev. B **89**, 235416 (2014).

[47] K. Saha, Photoinduced Chern insulating states in semi- Dirac materials, Phys. Rev. B **94**, 081103(R) (2016).

[48] R. Wang, B. Wang, R. Shen, L. Sheng, and D. Y. Xing, Floquet weyl semimetal induced by off-resonant light, Europhys. Lett. **105**, 17004 (2014).

[49] A. Lopez, Z. Z. Sun, and J. Schliemann, Floquet spin states in graphene under ac-driven spin-orbit interaction, Phys. Rev. B **85**, 205428 (2012).

[50] A. Lopez, A. Scholz, B. Santos, and J. Schliemann, Photoinduced pseudospin effects in silicene beyond the off-resonant condition, Phys. Rev. B **91**, 125105 (2015).

[51] T. Nag, S. Roy, A. Dutta, and D. Sen, Dynamical localization in a chain of hard core bosons under periodic driving, Phys. Rev. B **89**, 165425 (2014).

[52] A. Agarwala, U. Bhattacharya, A. Dutta, and D. Sen, Effects of periodic kicking on dispersion and wave packet dynamics in graphene, Phys. Rev. B **93**, 174301 (2016).

[53] SK. F. Islam and A. A. Zyuzin, Photoinduced interfacial chiral modes in threefold topological semimetal, Phys. Rev. B **100**, 165302 (2019).

[54] A. Bhattacharya and SK. F. Islam, Photoinduced spin-Hall resonance in a k^3-Rashba spin-orbit coupled two-dimensional hole system, Phys. Rev. B **104**, L081411 (2021).

[55] Y. Zhou and M. W. Wu, Optical response of graphene under intense terahertz fields, Phys. Rev. B **83**, 245436 (2011).

[56] A. Kundu and B. Seradjeh, Transport Signatures of Floquet Majorana Fermions in Driven Topological Superconductors, Phys. Rev. Lett. **111**, 136402 (2013).

[57] A. Kundu, H. A. Fertig, and B. Seradjeh, Effective Theory of Floquet Topological Transitions, Phys. Rev. Lett. **113**, 236803 (2014).

[58] M. Tahir and U. Schwingenschlögl, Tunable thermoelectricity in monolayers of MoS_2 and other group-VI dichalcogenides, New J. Phys. **16**, 115003 (2014).

[59] M. Tahir and P. Vasilopoulos, Off-resonant polarized light-controlled thermoelectric transport in ultrathin topological insulators, Phys. Rev. B **91**, 115311 (2015).

[60] S. Morina, O. V. Kibis, A. A. Pervishko, and I. A. Shelykh, Transport properties of a two-dimensional electron gas dressed by light, Phys. Rev. B **91**, 155312 (2015).

[61] A. A. Pervishko, O. V. Kibis, S. Morina, and I. A. Shelykh, Control of spin dynamics in a two-dimensional electron gas by electromagnetic dressing, Phys. Rev. B **92**, 205403 (2015).

[62] H. Dehghani, T. Oka, and A. Mitra, Out-of-equilibrium electrons and the hall conductance of a floquet topological insulator, Phys. Rev. B **91**, 155422 (2015).

[63] M. Genske and A. Rosch, Floquet-boltzmann equation for periodically driven fermi systems, Phys. Rev. A **92**, 062108 (2015).

[64] P. Titum, N. H. Lindner, M. C. Rechtsman, and G. Refael, Disorder-Induced Floquet Topological Insulators, Phys. Rev. Lett. **114**, 056801 (2015).

[65] P. Titum, N. H. Lindner, and G. Refael, Disorder-induced transitions in resonantly driven Floquet topological insulators, Phys. Rev. B **96**, 054207 (2017).

[66] M. Saha and D. Chowdhury, Anomalous thermoelectric properties of a floquet topological insulator with spin momentum non-orthogonality, J. Appl. Phys. **122**, 174301 (2017).

[67] I. Esin, M. S. Rudner, G. Refael, and N. H. Lindner, Quantized transport and steady states of floquet topological insulators, Phys. Rev. B **97**, 245401 (2018).

[68] SK. F. Islam and A. Saha, Driven conductance of an irradiated semi-Dirac material, Phys. Rev. B **98**, 235424 (2018).

[69] B. Sutherland, Localization of electronic wave functions due to local topology, Phys. Rev. B **34**, 5208 (1986).

[70] J. Vidal, R. Mosseri, and B. Doucot, Aharonov-Bohm Cages in Two-Dimensional Structures, Phys. Rev. Lett. **81**, 5888 (1998).

[71] C. C. Abilio, P. Butaud, T. Fournier, B. Pannetier, J. Vidal, S. Tedesco, and B. Dalzotto, Magnetic Field Induced Localization in a Two-Dimensional Superconducting Wire Network, Phys. Rev. Lett. **83**, 5102 (1999).

[72] D. Bercioux, D. F. Urban, H. Grabert, and W. Hausler, Massless Dirac-Weyl fermions in a $\mathcal{T}_3$ optical lattice, Phys. Rev. A **80**, 063603 (2009).

[73] F. Wang and Y. Ran, Nearly flat band with Chern number $C = 2$ on the dice lattice, Phys. Rev. B **84**, 241103(R) (2011).

[74] J. D. Malcolm and E. J. Nicol, Magneto-optics of massless kane fermions: Role of the flat band and unusual berry phase, Phys. Rev. B **92**, 035118 (2015).

[75] A. Raoux, M. Morigi, J. N. Fuchs, F. Piechon, and G. Montambaux, From Dia- to Paramagnetic Orbital Susceptibility of Massless Fermions, Phys. Rev. Lett. **112**, 026402 (2014).

[76] E. Illes, J. P. Carbotte, and E. J. Nicol, Hall quantization and optical conductivity evolution with variable Berry phase in the α-T_3 model, Phys. Rev. B **92**, 245410 (2015).

[77] T. Biswas and T. K. Ghosh, Magnetotransport properties of the α-T_3 model, J. Phys.: Condens. Matter **28**, 495302 (2016).

[78] D. F. Urban, D. Bercioux, M. Wimmer, and W. Häusler, Barrier transmission of dirac-like pseudospin-one particles, Phys. Rev. B **84**, 115136 (2011).

[79] E. Illes and E. J. Nicol, Klein tunneling in the α-T_3 model, Phys. Rev. B **95**, 235432 (2017).

[80] SK. F. Islam and P. Dutta, Valley-polarized magnetoconductivity and particle-hole symmetry breaking in a periodically modulated α-T_3 lattice, Phys. Rev. B **96**, 045418 (2017).

[81] T. Biswas and T. K. Ghosh, Dynamics of a quasiparticle in the α-T_3 model: role of pseudospin polarization and transverse magnetic field on zitterbewegung, J. Phys.: Condens. Matter **30**, 075301 (2018).

[82] J. D. Malcolm and E. J. Nicol, Frequency-dependent polarizability, plasmons, and screening in the two-dimensional pseudospin-1 dice lattice, Phys. Rev. B **93**, 165433 (2016).

[83] A. Balassis, D. Dahal, G. Gumbs, A. Iurov, D. Huang, and O. Roslyak, Magnetoplasmons for the α-T_3 model with filled Landau levels, J. Phys.: Condens. Matter **32**, 485301 (2020).

[84] A. Iurov, G. Gumbs, and D. Huang, Many-body effects and optical properties of single and double layer α-T_3 lattices, J. Phys.: Condens. Matter **32**, 415303 (2020).

[85] A. Iurov, L. Zhemchuzhna, G. Gumbs, D. Huang, D. Dahal, and Y. Abranyos, Finite-temperature plasmons, damping, and collective behavior in the $\alpha-\mathcal{T}_3$ model, Phys. Rev. B **105**, 245414 (2022).

[86] E. Illes and E. J. Nicol, Magnetic properties of the α-T_3 model: Magneto-optical conductivity and the Hofstadter butterfly, Phys. Rev. B **94**, 125435 (2016).

[87] A. D. Kovacs, G. David, B. Dora, and J. Cserti, Frequency-dependent magneto-optical conductivity in the generalized α-T_3 model, Phys. Rev. B **95**, 035414 (2017).

[88] Y. R. Chen, Y. Xu, J. Wang, J. F. Liu, and Z. Ma, Enhanced magneto-optical response due to the flat band in

nanoribbons made from the α-T_3 lattice, Phys. Rev. B **99**, 045420 (2019).

[89] L. Chen, J. Zuber, Z. Ma, and C. Zhang, Nonlinear optical response of the α-T_3 model due to the nontrivial topology of the band dispersion, Phys. Rev. B **100**, 035440 (2019).

[90] D. O. Oriekhov and V. P. Gusynin, RKKY interaction in a doped pseudospin-1 fermion system at finite temperature, Phys. Rev. B **101**, 235162 (2020).

[91] O. Roslyak, G. Gumbs, A. Balassis, and H. Elsayed, Effect of magnetic field and chemical potential on the RKKY interaction in the α-T_3 lattice, Phys. Rev. B **103**, 075418 (2021).

[92] J. Wang, J. F. Liu, and C. S. Ting, Recovered minimal conductivity in the α-T_3 model, Phys. Rev. B **101**, 205420 (2020).

[93] B. Dey, P. Kapri, O. Pal, and T. K. Ghosh, Unconventional phases in a haldane model of dice lattice, Phys. Rev. B **101**, 235406 (2020).

[94] J. Wang and J. F. Liu, Quantum spin Hall phase transition in the α-T_3 lattice, Phys. Rev. B **103**, 075419 (2021).

[95] B. Dey and T. K. Ghosh, Photoinduced valley and electron-hole symmetry breaking in $\alpha-T_3$ lattice: The role of a variable Berry phase, Phys. Rev. B **98**, 075422 (2018).

[96] B. Dey and T. K. Ghosh, Floquet topological transition in the $\alpha-T_3$ lattice, Phys. Rev. B **99**, 205429 (2019).

[97] A. Iurov, G. Gumbs, and D. Huang, Peculiar electronic states, symmetries, and Berry phases in irradiated α-T_3 materials, Phys. Rev. B **99**, 205135 (2019).

[98] M. A. Mojarro, V. G. Ibarra-Sierra, J. C. Sandoval-Santana, R. Carrillo-Bastos, and G. G. Naumis, Electron transitions for Dirac Hamiltonians with flat bands under electromagnetic radiation: Application to the α-T_3 graphene model, Phys. Rev. B **101**, 165305 (2020).

[99] L. Tamang, T. Nag, and T. Biswas, Floquet engineering of low-energy dispersions and dynamical localization in a periodically kicked three-band system, Phys. Rev. B **104**, 174308 (2021).

[100] Z. P. Niu and S. Jun Wang, Valley polarized transport and negative differential resistance in an irradiated α-T_3 lattice, J. Phys. D: Appl. Phys. **55**, 255303 (2022).

[101] M. Bukova, L. DAlessio, and A. Polkovnikov, Universal high-frequency behavior of periodically driven systems: From dynamical stabilization to Floquet engineering, Adv. Phys. **64**, 139 (2015).

[102] I. Souza and D. Vanderbilt, Dichroic f-sum rule and the orbital magnetization of crystals, Phys. Rev. B **77**, 054438 (2008).

[103] W. Yao, D. Xiao, and Q. Niu, Valley-dependent optoelectronics from inversion symmetry breaking, Phys. Rev. B **77**, 235406 (2008).

[104] D. L. Bergman and V. Oganesyan, Theory of Dissipationless Nernst Effects, Phys. Rev. Lett. **104**, 066601 (2010).

[105] R. Karplus and J. M. Luttinger, Hall effect in ferromagnetics, Phys. Rev. **95**, 1154 (1954).